

<https://doi.org/10.1038/s43247-024-01419-2>

# Energetic particle precipitation influences global secondary ozone distribution

Check for updates

Jia Jia <sup>1,2</sup> , Lise E. Murberg <sup>1,3</sup>, Tiril Løvset<sup>1</sup>, Yvan J. Orsolini <sup>1,2,3</sup>, Patrick J. Espy <sup>1,2</sup>, Lilou C. G. Zeller<sup>1,4</sup>, Cornelius Csar Jude H. Salinas<sup>5,6</sup>, Jae N. Lee <sup>5,6</sup>, Dong Wu<sup>5</sup> & Jiarong Zhang <sup>7</sup>

The secondary ozone layer is a global peak in ozone abundance in the upper mesosphere-lower thermosphere (UMLT) around 90–95 km. The effect of energetic particle precipitation (EPP) from geomagnetic processes on this UMLT ozone remains largely unexplored. In this research we investigated how the secondary ozone responds to EPP using satellite observations. In addition, the residual Mean Meridional Circulation (MMC) derived from model simulations and the atomic oxygen [O], atomic hydrogen [H], temperature measurements from satellite observations were used to characterise the residual circulation changes during EPP events. We report regions of secondary ozone enhancement or deficit across low, mid and high latitudes as a result of global circulation and transport changes induced by EPP. The results are supported by a sensitivity test using an empirical model.

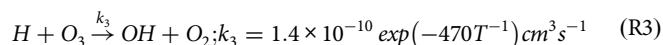
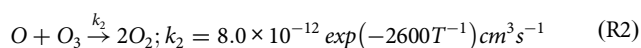
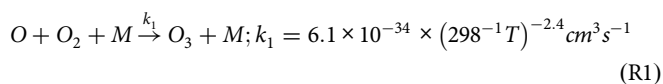
Energetic particle precipitation (EPP) refers to the processes by which highly energetic protons, electrons and ions enter the atmosphere. These particles are emitted by the sun during e.g., solar flares, coronal mass ejections (CMEs) or from the Earth's radiation belts after perturbations by solar wind fluctuations and magnetospheric processes. Trapped by the Earth's magnetic field, the particles are then accelerated and precipitate into the polar regions of the upper atmosphere. Due to the many processes at play, EPP displays high variability in its temporal flux and energy distribution, ranging from the sub-daily timescale (e.g., linked to auroral oval precession, magnetospheric waves) to the decadal time scale (e.g., linked to the 11-year solar cycle). Through the deposition of their energy, ranging from <10 keV to a few hundred MeV, EPP instigates dissociation and ionisation and subsequent ionic and neutral chemistry<sup>1–4</sup> at various altitudes (~30–120 km) within the atmosphere. This leads to modifications in the atmospheric background chemistry, which leads, in particular, to the depletion of ozone<sup>5–9</sup>. This is due to the fact that EPP is the main source of NO<sub>x</sub> (NO, NO<sub>2</sub>) above the middle stratosphere at high latitudes, and the NO<sub>x</sub>-driven catalytic cycle, in the presence of sunlight, is the dominant ozone-depleting cycle in the mid and upper stratosphere. Satellite and ground-based observations have demonstrated that EPP leads to ozone depletion in the stratospheric ozone layer, more specifically in the mid and upper stratosphere at polar and sub-polar latitudes. The HO<sub>x</sub> (OH, HO<sub>2</sub>)-driven cata-

lytic cycle also plays an important role in the ozone concentrations in the mesosphere, where it affects the transient tertiary ozone layer<sup>10</sup>. These findings have been corroborated by model investigations<sup>8,11–15</sup>.

In addition to the permanent primary and transient tertiary ozone layers, there exists another permanent peak in global ozone abundance, known as the secondary ozone layer, located in the upper mesosphere–lower thermosphere (UMLT) around 90–100 km altitude. As the secondary ozone layer is our research target, to facilitate the comprehension of the obtained results, we first provide a concise overview of the chemistry governing the abundance of ozone in this layer. The abundance of ozone in the UMLT undergoes significant variations due to the process of photodissociation by sunlight, resulting in lower ozone levels during daytime. It also exhibits rapid changes during twilight periods. While photodissociation reduces ozone levels in this layer to ~0.7–1.2 ppmv during the day, the nighttime values range from 6 to 21 ppmv<sup>16</sup>. The nighttime secondary ozone layer exists in a state of chemical equilibrium with a short lifetime of minutes, regulated by temperature and the presence of the longer-lived species atomic hydrogen [H] and oxygen [O] that act as the main chemical sinks and sources<sup>16</sup>. Hence, it cannot be considered as a transported trace species as in the stratosphere. Our analysis exclusively focuses on nighttime conditions, when ozone is more abundant and in a simpler state of chemical equilibrium.

<sup>1</sup>Norwegian University of Science and Technology (NTNU), Trondheim, Norway. <sup>2</sup>Birkeland Center for Space Science (BCSS), Bergen, Norway. <sup>3</sup>NILU- Climate and Environmental Research Institute, Kjeller, Norway. <sup>4</sup>ENSTA-Paris, Palaiseau, France. <sup>5</sup>Goddard Space Flight Center, Greenbelt, MD, USA. <sup>6</sup>University of Maryland, Baltimore County, MD, USA. <sup>7</sup>Clemson University, Clemson, SC, USA. e-mail: [jia.jia@ntnu.no](mailto:jia.jia@ntnu.no)

The following reactions and their corresponding reaction rates drive the production and destruction of secondary ozone during nighttime:



where the rates  $k_1$  to  $k_3$  denote the rate coefficients for the reactions<sup>17</sup>, and  $M$  represents a third body that facilitates the collision process. This leads to a steady-state equilibrium formula for the ozone concentration during night<sup>16,18–20</sup> given by

$$O_3 = \frac{k_1[O][O_2][M]}{k_2[O] + k_3[H]} \quad (1)$$

While  $[O]$  appears as both a source and a sink of ozone, (R2) is a slower reaction than (R3), which predominantly governs the loss of nighttime ozone in the winter UMLT conditions considered here. Consequently, the equilibrium concentration of nighttime ozone is inversely proportional to the density of atomic hydrogen  $[H]$  and proportional to  $[O]$  and  $[O_2]$ . Furthermore, the destruction reaction rates,  $k_2$  and  $k_3$ , are positively related to the temperature ( $T$ ), whereas the rate of creation reaction ( $k_1$ ) is negatively related to temperature<sup>16</sup>. These relationships imply that higher temperatures result in slower ozone creation rates, coupled with elevated ozone destruction rates. Consequently, increasing temperature leads to lower equilibrium ozone concentrations.

$NO_x$  and  $HO_x$  that can be enhanced by EPP do not play a significant role in the vicinity of the ozone secondary maximum. Generation of  $HO_x$  relies on the existence of the water clusters that are absent in UMLT. And EPP-generated  $NO_x$  cannot effectively compete with  $[H]$  in destructing ozone in the UMLT<sup>16</sup> due to the fact that the reaction rate of  $NO$  and ozone,  $3 \times 10^{-12} \exp(-1500T^{-1}) \text{ s}^{-1}$ <sup>17</sup>, is hundreds to a thousand times slower than  $k_3$  under UMLT conditions. Thus, in UMLT it is not the  $NO_x$  and  $HO_x$  chemistry affecting the product ozone, but rather the chemistry of the reagents,  $[O]$  and  $[H]$ , that themselves could be affected by transport. The response of the secondary ozone layer to EPP has received very little attention thus far based on this chemical perspective. However, the influence of EPP in the UMLT may manifest through changes in temperature and atmospheric circulation: In the presence of significant auroral activity, polar mean meridional circulation (MMC) cells develop, driven by auroral heating, that are characterised by ascent at high latitudes<sup>21</sup>. Hence, despite the insensitivity of nighttime ozone to the  $NO_x$  and  $HO_x$ -driven catalytic cycles in the UMLT, indirect effects of EPP on the secondary ozone layer may arise through temperature and circulation-induced changes in longer-lived source/sink species, namely  $[O]$  and  $[H]$ . Exploration of this indirect impact of EPP on the secondary ozone layer remains largely unexplored.

To gain insight into the potential circulation-induced changes, the present study focuses on investigating the variations in the secondary ozone layer associated with EPP during the boreal and austral winters. We quantify the nighttime secondary ozone variability across latitudes associated with EPP, as measured by the daily  $A_p$  index, using satellite ozone observations from the sounding of the atmosphere using broadband emission radiometry (SABER) and microwave limb sounder (MLS) instruments. To gain a comprehensive understanding of the circulation changes that indirectly influence ozone abundance, the SABER satellite data of temperature, atomic hydrogen  $[H]$ , and atomic oxygen  $[O]$  are complemented by diagnostics of simulations with the extended Whole Atmosphere Community Climate Model WACCM-X and the Naval Research Laboratory Mass Spectrometer

and Incoherent Scatter Radar Model 2.0 (NRLMSIS 2.0). Our analysis highlights the global nighttime variability of the secondary ozone layer resulting from EPP, shedding light on the underlying mechanisms driving these variations.

## Results

### EPP signal in satellite secondary ozone measurements

The results of the multiple linear regression (MLR) fitting using SABER daily zonal mean ozone data from 25 January 2002 to 31 December 2019, focusing on boreal winters (December–February), are presented in Fig. 1. The upper panels of Fig. 1 depict the global zonal-mean variations in ozone attributed to EPP (Fig. 1a) and solar irradiance variations (Fig. 1b). These variations are derived from the fitted coefficients, representing the effect of a single unit index (1 Ap and 1 sfu). Our research findings align with previous studies based on MLS data, as reported by Lee and Wu<sup>22</sup>, regarding the relationship between secondary ozone variations and solar irradiance. That is the change of nighttime ozone can exceed 1 ppmv/100 sfu in the polar winter hemisphere. However, the notable aspect of our study lies in the investigation of the impact of EPP on secondary ozone. As shown in Fig. 1a, for DJF, we observe a decrease in the upper part of the secondary ozone layer in the northern hemisphere polar region due to EPP. Surprisingly, the influence of EPP extends beyond the polar regions and leads to an enhancement of ozone in the tropical region where, remarkably, the magnitudes of EPP-induced ozone variations are comparable to those caused by solar irradiance per unit index (Fig. 1b). In the polar region on the other hand, the EPP-induced contribution opposes the solar irradiance contribution, highlighting the complex and non-local nature of EPP-induced effects on secondary ozone distribution. Similar responses are observed in austral winter (JJA, Fig. S1) as well.

The observed (nighttime) ozone responses in our study are considered to occur within a day, as we fitted daily mean indices without incorporating any time lag. We do not anticipate observing stratospheric ozone responses to EPP since the downward transport of  $NO_x$  typically requires a longer time frame (typically taking months). Additionally, the Solar Proton Events that are capable of directly enhancing stratospheric  $NO_x$  are too sporadic to detect a signal in the statistical analysis. However, it is worth noting that the tertiary ozone layer, which is directly influenced by EPP, exhibits a distinct signal of depletion, as expected.

To eliminate the possible artificial responses yielded by the regular 60-day yaw effect (see the section “Methods”) in SABER measurements and to ensure the robustness of our findings, we conducted a parallel analysis using ozone measurements from MLS. The ozone responses to EPP observed in MLS data in the valid height range of the MLS data (i.e., below  $10^{-3}$  hPa height) align closely with those obtained from SABER. The ozone response derived from MLS measurements is presented in Fig. S2, providing additional support and consistency to our findings.

To compare with the results obtained from a compositing method (High-Ap vs. Low-Ap, depicted in Fig. 1c), the  $A_p$  and F10.7 contributions using the MLR method are combined and shown in Fig. 1d. In the High-Ap vs. Low-Ap approach, the thresholds for high and low  $A_p$  values are determined by the 95- and 5-percentiles, respectively, resulting in  $A_{p_{\text{high}}} \geq 28$  and  $A_{p_{\text{low}}} \leq 2$ . The result shown in Fig. 1c is obtained by calculating the difference between the mean ozone values during high  $A_p$  and low  $A_p$  conditions. The combined contributions of  $A_p$  and F10.7 using the MLR method (Fig. 1d) are determined by the fitted coefficients times the differences between the median values of the indices (32 for  $A_p$  and 26 for F10.7) during high- $A_p$  and low- $A_p$  conditions (i.e., storm time period and quiet time period) in boreal winters throughout the observation period. The agreement between Fig. 1c and d reinforces the reliability of MLR and the fact that the secondary ozone changes obtained through the High- $A_p$  vs. Low- $A_p$  comparison yield a combined influence of EPP and solar irradiance. In the following analysis, we employ the median  $A_p$  difference between high- $A_p$  and low- $A_p$  conditions, specifically the value of 32, to represent the average impact of EPP on various species and variables.

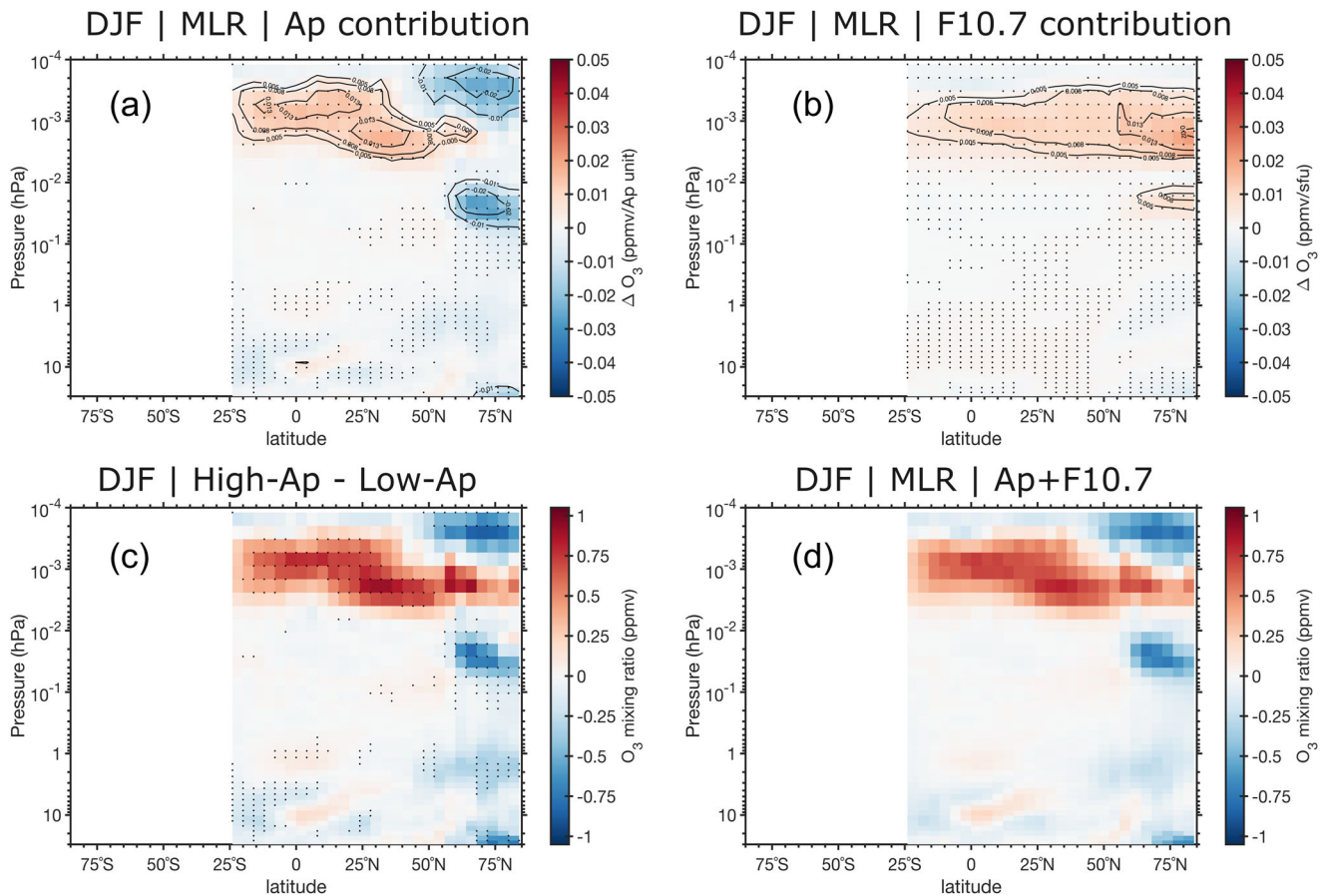


**Fig. 1 | Boreal winter zonal-mean nighttime SABER ozone variations along pressure levels.** Ozone variations from **a** EPP and **b** solar irradiance contributions (depicted as changes in ppmv per unit Ap and F10.7) using the MLR method in SABER data. Panel **c** shows the difference in ozone mean between High-Ap and Low-Ap days, while panel **d** presents the combined contributions of Ap and F10.7

based on fitted coefficients and median index value differences (32 for Ap and 26 for F10.7) between high-Ap and low-Ap conditions throughout the observation period. Significant signals (95% confidence, derived from Student's *t*-test in **(a)**, **(b)** and from Monte Carlo test via randomise the High-Ap dates 20000 times in **(c)**) are marked as black dots.

**Understanding the secondary ozone changes by EPP-circulation variation**

To investigate the potential relationship between circulation patterns and the observed variations in secondary ozone, we examined changes in the residual MMC across the mesosphere–lower thermosphere region in response to EPP. Figure 2 displays the velocity stream function (a–c) and, in order to highlight the meridional flow, the meridional advection component  $\bar{v}^*$  (d–f) in boreal winters, as calculated from SD-WACCM-X simulations.

The climatological residual MMC and the meridional component  $\bar{v}^*$  in the thermosphere, as depicted in Fig. 2a, d, are primarily driven by solar extreme ultraviolet (EUV) heating. This circulation pattern facilitates the transport of trace species, including the sources and sinks of secondary ozone ([O], [H]), through upwelling in the summer hemisphere and downwelling in the winter hemisphere, resulting in a clockwise hemispheric circulation during boreal winters<sup>21</sup>. In the mesosphere, the familiar mesospheric residual MMC pattern from the summer pole to the winter pole is driven by gravity wave drag<sup>23</sup>. Situated between the thermospheric and mesospheric circulation cells, a lower thermospheric reverse circulation appears (Fig. 2a). It is characterised by a flow in a thin layer towards the summer pole, centred near 10<sup>-4</sup> hPa (Fig. 2d), while flow towards the winter pole prevails above and below, ensuring the closure of the circulations and maintains the continuity of mass flow<sup>24–27</sup>. This circulation is thicker in the summer hemisphere than in the winter hemisphere and extends from the summer pole across the winter hemisphere mid-latitudes.

In the presence of significant auroral activity, as illustrated in Fig. 2b, e, an additional MMC cell driven by auroral heating appears in the winter

hemisphere. This MMC is characterised by an ascent at high latitudes (near ~75°) and a descent at mid-latitudes, hence opposing and compressing the climatological interhemispheric thermospheric MMC that previously extended to the pole in the absence of EPP. This perturbed aurora-driven circulation is confined to high latitudes, but the exact meridional boundary between the two—climatological and perturbed—opposing circulation cells depends on geographic longitude and the level of magnetic activity<sup>21</sup>. Our result shows that the statistical meridional boundary above 10<sup>-4</sup> hPa is ~50° in the winter hemisphere. The changes described above are more prominently illustrated in Fig. 2c, f, which presents the Ap component of MMC at an Ap-index of 32 derived using the MLR method. We observe notable circulation changes spanning the entire latitude range. Our result shows that, in the winter hemisphere, the perturbed auroral circulation affects the circulation differently above and below 10<sup>-4</sup> hPa. Above, vertical motions correspond to descent near ~50°N and ascent near ~80°N. Just below 10<sup>-4</sup> hPa (see the arrows in Fig. 2b, c), the bottom of the aurora-driven cell in high Ap conditions interferes with the background lower thermospheric residual MMC: near ~50°N, the horizontally divergent flow (with a poleward branch north of ~50°, and a return flow toward the summer pole south of ~50°) is intensified. Although variations are not always significant, perturbations are observed in UMLT. Note simultaneously, that in the summer hemisphere, similar aurora-induced heating and ascent at high latitudes reinforce the background thermospheric MMC as well (Fig. 2c).

However, we want to stress that the simulation run utilised here did not incorporate medium-energy electrons (MEE, with energies between 10 keV to several MeV). Consequently, the results presented here may not provide a

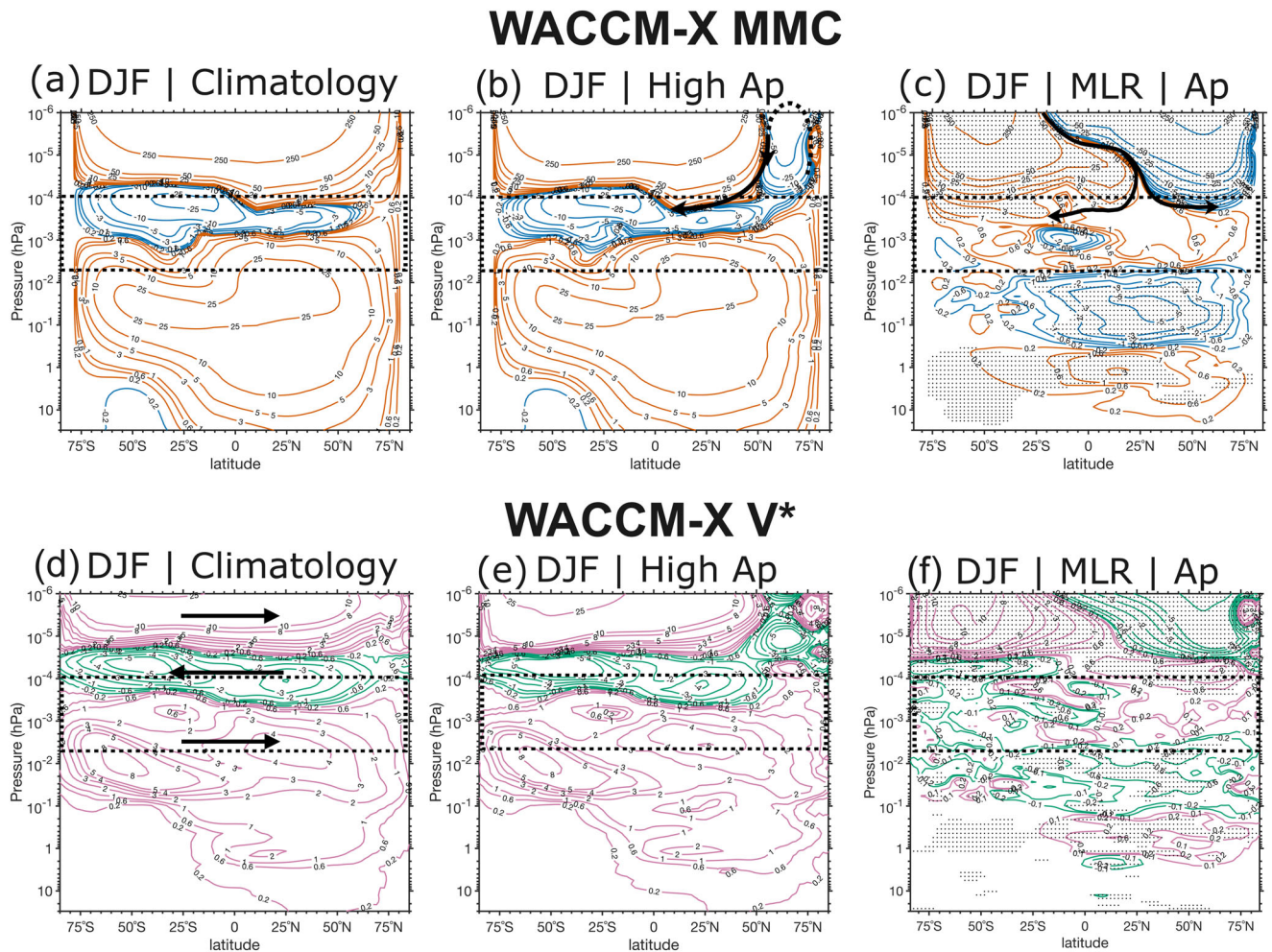


**Fig. 2 | Residual MMC and its meridional flow component  $\bar{v}^*$  along latitude and pressure levels from SD-WACCM-X simulations. a and d** Climatology. **b and e** Mean values during the High-Ap days. **c and f** EPP induced circulation anomalies at High-Ap situations calculated using MLR method at Ap value 32. **a–c** negative values/blue contours represent the anti-clockwise circulation; positive values/orange

contours represent the clockwise circulation. **d–f** negative values/green contours represent the southward motion; positive values/pink contours represent the northward motion. Black arrows indicate the flow direction. The black dashed boxes mark the relevant secondary ozone layer. Units in **a–c** are  $10^{-4} \text{ m s}^{-1}$  and in **d–f** are  $\text{m s}^{-1}$ . Significant signals (95% confidence) are marked as black dots.

comprehensive depiction of EPP contribution to the circulation above 60 km.

### Understanding the secondary ozone changes by EPP–species variation

In UMLT, the chemical lifetime of [O] ranges from  $10^5$  to  $10^7$  s, [H] has lifetimes ranging from  $10^3$  to  $10^5$  s, while the lifetime of the odd hydrogen family (predominantly comprising [H] at these heights) is longer than  $10^6$  s<sup>28–31</sup>. These lifetimes are comparable to or larger than dynamical time scales. Therefore, transport effects are important for [O] and [H] in UMLT. The suggested alteration in circulation patterns discussed earlier, along with the increased polar thermosphere temperature due to auroral heating, can significantly influence the nighttime abundance of ozone in the secondary layer by impacting the levels of [O] and [H] and their reaction rates (refer to introduction). To further validate the inferences about transport based on SD-WACCM-X simulations, we conducted an MLR analysis of the response of [O], [H], and temperature (*T*) to EPP using SABER observations (Fig. 3a, c, e). The background climatology of the variables is presented in Fig. 3b, d, f, providing context for understanding the variations in their values associated with changes in circulation patterns.

Over the relevant layer (dashed box), under high Ap conditions, we observe an enhancement of [O] over a broad range of latitudes from the summer subtropics to the winter sub-polar latitudes, with the exception of a

narrow region near the pole. On the other hand, we observe a decrease in [H], especially in the upper part of the layer, across the subtropics, fading in the mid-latitudes of the winter hemisphere and then increasing poleward. The temperature increases mainly over high latitudes. The changes in [O], favouring ozone increase, are consistent with a stronger downward flow aloft, as suggested by the Ap-perturbed lower thermospheric residual MMC (arrows in Fig. 2c), which extends into southern latitudes. On the other hand, near the top of that layer, the lower thermospheric residual circulation also shows a weak anomalous equator-ward flow across the northern subtropics, reinforcing the background return flow that advects southward [H]-poor air from the winter high latitudes, where [H] is less abundant (see climatological gradient in Fig. 3f). With more ozone formation from the increased [O] and less ozone depletion from the decreased [H], a new ozone equilibrium is established, resulting in an enhancement of secondary ozone abundance at the mid and low latitudes.

In the polar thermosphere, the influence of an Ap-index change of 32 leads to auroral heating, resulting in a temperature increase of approximately 10–20 K at the pressure level of  $10^{-3}$ – $10^{-4}$  hPa. This temperature enhancement aligns with previous studies<sup>32–34</sup> leading to a suppression of ozone formation processes and an acceleration of the ozone-depleting reactions. The SABER-derived products [O] and [H] also reveal an increase in their mixing ratios, which are qualitatively consistent with the downward transport occurring around 50°N above  $10^{-4}$  hPa and the poleward

# SABER [O] T [H]

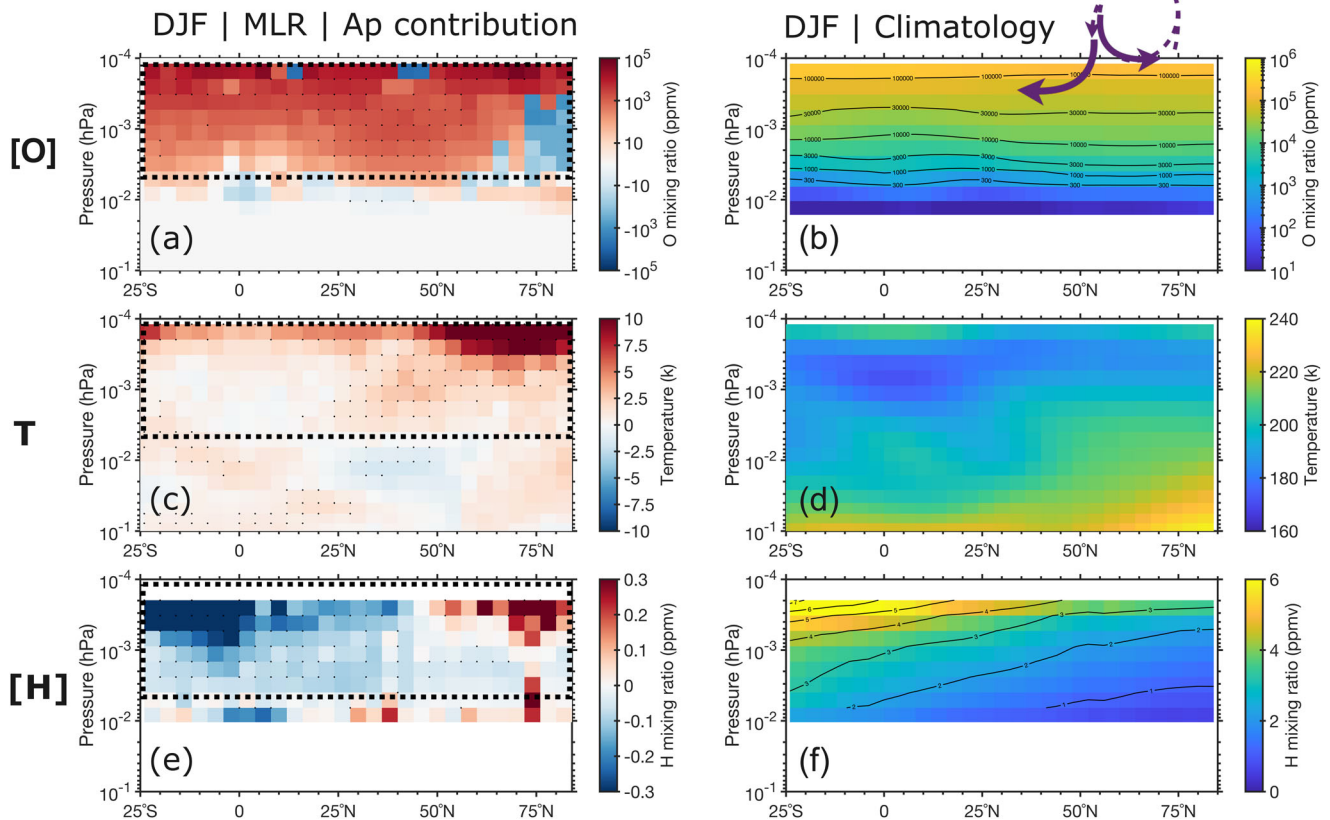


**Fig. 3 | Boreal winter zonal-mean nighttime [O], temperature T, and [H] variations along pressure levels from SABER. a, c and e** EPP contributions (depicted as changes in ppmv per 32 units Ap) using the MLR method. **b, d and f** Corresponding climatology. The black dashed boxes mark the relevant secondary

ozone layer. Black arrows that indicate the circulation anomaly due to EPP in Fig. 2 are overlapped in (b) as purple arrows. Significant signals (95% confidence) are marked as black dots.

transport induced by the aurora-driven anticlockwise flow. Consequently, both ozone formation and depletion are enhanced. We have to mention, though, that the usage of SABER [O] and [H] is generally confined to pressures greater than  $3 \times 10^{-4}$  hPa. Similar to the mid and low latitudes, a new ozone equilibrium is formed in the high latitudes of the winter hemisphere. While we observed a decrease in the abundance of secondary ozone at the winter pole, it remains unclear which contribution (e.g., from T, [H] or [O]) governs this decrease. To address this question, we conducted a chemical simulation using the NRLMSIS 2.0 model (hereafter MSIS).

MSIS is an empirical model providing information on the temperature, density and atmospheric composition from the ground to the exobase based on the day of the year, solar flux and Ap index input<sup>35</sup>. Ozone is not a standard output of the model. The ozone profiles in the secondary layer region are calculated from [O], [O<sub>2</sub>], [H], T and air density output from MSIS assuming the equilibrium Eq. (1). In the MSIS simulation (Fig. 4a, c), the “true” values of ozone changes are calculated by multiplying the MSIS winter climatology profile in the latitude bin of interest (in this case, 16°N and 68°N) with the ozone changes expressed as a percentage obtained from SABER analysis using MLR with an Ap value of 32. To ensure a consistent baseline, we compared the MSIS climatology and the SABER climatology. The outcomes are depicted in Fig. 4b, d, illustrating a good consistency. To simulate the individual contributions of T, [O], and [H] to the ozone variations, a recalibration of the equilibrium ozone profile is performed by keeping the climatological parameters, such as species mixing ratio, air density, and T, with the exception of the specific parameter being investigated. For the latter, to represent the EPP effect, a height-dependent percentage change is applied to the climatology based on the SABER observations. For instance, the impact of temperature change is calculated

by considering the climatological values of [O], [O<sub>2</sub>], [H], and air density, while the temperature component’s climatological value is replaced by a value that incorporates the percentage changes resulting from EPP, as obtained from SABER’s MLR analysis (Fig. 3c). This approach, similar to the one in Tweedy et al.<sup>21</sup>, allows for the isolation and evaluation of the individual effects of T, [O], and [H] on ozone variations.

The variable contribution to ozone changes in the mid-low latitudes and in the high latitudes are shown in Fig. 4a, c. In the low latitudes, the observed ozone variation depicted in Fig. 1 can be attributed to the combined changes in [O] and [H], with minimal temperature variations (<2 K). Conversely, in the high latitudes, the reduction in ozone can predominantly be attributed to the temperature increase resulting from auroral heating. However, it is worth noting that at the winter pole, our simulations indicate a larger decrease in ozone compared to the “true” ozone variation. We suspect that the discrepancy can be attributed to the nonlinearity of the temperature-ozone relationship and the usage of mean values over a large number of events as inputs in the MSIS simulation, which may not capture the full range of variability. Besides, the potential overestimation of the polar temperature response to EPP, calculated from SABER data compared to other data sources such as MIPAS measurements<sup>32</sup>, could contribute to the observed overestimation of the ozone deficit as well. Our MSIS simulation indicates that if the entire disagreement arises from the overestimation of EPP-induced temperature derived from SABER, it is overestimated by a factor of ~1.6 in the UMLT region.

## Discussion

This study focuses on investigating the secondary ozone response to EPP using satellite observations obtained from SABER and MLS. Our analysis

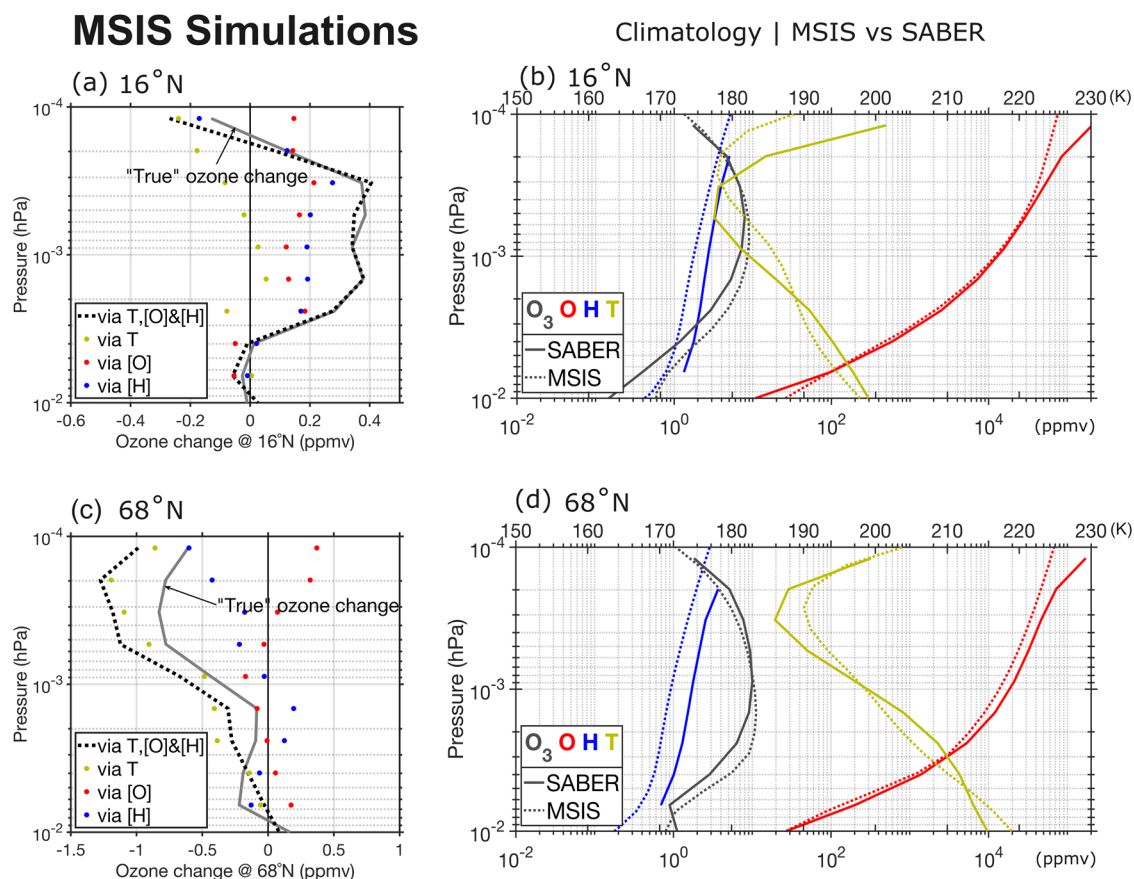


**Fig. 4 | Zonal mean ozone changes simulated by MSIS empirical model due to variations in  $T$ ,  $[O]$ , and  $[H]$  at Ap value 32, and the corresponding climatology. **a, b** at  $16^\circ\text{N}$ . **c, d** at  $68^\circ\text{N}$ . **a, c** The grey solid lines indicate the “true” values of ozone changes, obtained by multiplying the MSIS winter climatology profile in the respective latitude bin with the percentage ozone changes derived from SABER analysis using MLR with an Ap value of 32. The individual contributions of  $T$ ,  $[O]$ ,**

**and  $[H]$  to ozone variations are represented by the coloured dots, where the model input of the targeted parameter is modified based on the percentage changes observed in the corresponding variables derived from SABER data. The combined contributions of these factors are depicted by the dash-dotted black lines. **b** and **d** illustrate the climatology of  $[O]$ ,  $[H]$ ,  $T$  and ozone from MSIS and SABER at  $16^\circ\text{N}$  and  $68^\circ\text{N}$ .**

reveals a significant decrease in the upper secondary ozone layer in polar regions. Moreover, surprisingly, both SABER and MLS observations provide robust evidence of an enhanced secondary ozone response extending from the winter hemisphere’s mid-latitudes across the tropics into the summer hemisphere subtropics.

To ensure that the observed signal is attributed to EPP rather than solar irradiance variations, we employed several methods to separate their respective impacts on secondary ozone. In this report, we present the outcomes obtained through the MLR method, where we concurrently fitted the daily Ap-index and F10.7-index. Thorough examinations were performed to validate the findings (refer to the method and supplementary material for details). We observed a consistent secondary ozone response, further confirming that the observed response is primarily induced by EPP rather than solar irradiance.

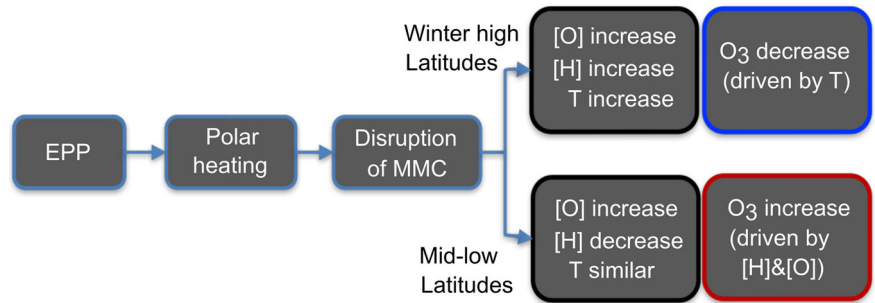
Considering that the nighttime secondary ozone is not expected to undergo chemical changes through catalytic reactions related to the EPP-induced enhancement of  $\text{HO}_x$  and  $\text{NO}_x$ , we examined the variations in the MMC induced by EPP using supporting simulations carried out with specified-dynamics WACCM-X simulations. We investigated the potential relationship between these MMC variations and the observed ozone responses by analysing satellite data of  $[O]$ ,  $[H]$ , and temperature obtained from SABER. Our analysis revealed that the EPP-induced perturbed MMC circulation at high latitudes during winter interferes with the lower thermospheric MMC, leading to their merging into a larger circulation pattern. Consequently, a downward flow is induced at the boundary between the climatological and the opposing EEP-perturbed circulation cells, where a

divergent horizontal flow is strengthened. At the latitude where the flow is divergent, pathways are created for the poleward transport of long-lived  $[O]$  and  $[H]$  toward high latitudes and for their equator-ward transport toward low latitudes. Combined with the auroral heating in the polar thermosphere, the altered abundances of  $[O]$  and  $[H]$  dictate the establishment of new ozone equilibrium values. These changes result in an enhancement of the secondary ozone signal at mid and low latitudes (dominated by changes in  $[H]$  and  $[O]$ ) while decreasing the values of secondary ozone at high latitudes (dominated by the increased temperature). Figure 5 summarises the mechanisms described above.

The proposed mechanism offers additional insights into the diminished signal observed in the southern hemisphere winter compared to the northern hemisphere, as evident in both SABER and MLS datasets (Figs. S1, S2). The hemispheric asymmetry of the seasonally varying background MMC (Fig. S6) is a contributing factor influencing the disturbance induced by EPP. Moreover, the magnetic pole’s displacement from the geometric pole in the southern hemisphere introduces variations in the EPP forcing compared to the northern hemisphere. Further investigation into these aspects is needed to enhance our understanding.

We encountered challenges in conducting case studies or employing statistical methods such as superposed epoch analysis to further investigate the findings. The variable nature of solar irradiance on a 27-day basis makes it difficult to establish specific cases or perform certain kinds of statistical analyses to study EPP’s contribution to secondary ozone changes (see Fig. S3 in the supplementary). However, our study reveals a significant statistical secondary ozone response to general geomagnetic storms when compared

**Fig. 5 | Summary diagram depicting the mechanism underlying EPP-induced secondary ozone variations.** This diagram summarises the mechanisms we have presented. Polar ozone depletion is suggested to be caused by aurora heating-induced changes in reaction rates, while the ozone enhancement in the mid-low latitudes is suggested to result from changes in [O] and [H] due to transport.



to the climatological conditions. These results emphasise the substantial impact of EPP on the equilibrium of secondary ozone, which exhibits a similar magnitude of influence per unit as solar irradiance.

While our findings highlight the complex interplay between EPP-induced circulation patterns, chemical processes, and the distribution of ozone in the UMLT region, it is important to acknowledge the limitations of our research and the need for further investigations to validate our suggested mechanism through model simulations. One minor limitation relates to the SABER data. The use of SABER [O] and [H] is generally restricted to pressures  $>3 \times 10^{-4}$  hPa ( $\sim 100$  km) due to the increased uncertainty in SABER temperatures above 100 km and the weak airglow emissions above 100 km on which the retrieval relies. This introduces some uncertainties in our high-latitude UMLT ozone response to EPP, as depicted in Fig. 4c. In addition, we did not differentiate the portion of [O] directly produced by EPP through ion-neutral chemistry from the one due to transport, an aspect deserving further confirmation. Besides, the WACCM-X simulation run utilised here did not incorporate medium-energy electrons (MEE, with energies between 10 keV to several MeV). Consequently, the presented model results may not provide a comprehensive depiction of EPP effects above 60 km<sup>13</sup>.

Furthermore, this first investigation does not delve into the detailed quantification of the secondary ozone budget in WACCM-X due to contributions from eddy diffusion (from unresolved scales), eddy flux (from resolved scales), molecular diffusion, or meridional advection and vertical advection. Such a detailed examination would be necessary to unravel the precise causes of changes in [O] and [H], ultimately influencing ozone variations in the mid-low latitudes. A recent paper by Wang et al.<sup>36</sup> focusing on the climatological distribution of [O] using SD-WACCM-X indicates that the primary forcing term for [O] is vertical advection in the polar region. Similar investigations, including a detailed ozone budget, would be required to quantify EPP-induced changes in forcing terms and their respective contributions to both [O] and [H]. We propose, as a plausible qualitative explanation, that the aurorally induced cell interacts with the lower thermospheric circulation, resulting in changes in [O] and [H] that impact ozone levels. Undertaking a more comprehensive set of simulations, providing detailed constituent output for budget studies would be justified as a continuation of the present observation-guided study.

## Methods

### SABER

The SABER instrument onboard NASA’s TIMED satellite is an infra-red radiometer that follows a circular orbit with an inclination of 74.1°. With a daily precess-orbit adjustment of  $\sim 3^\circ$  relative to the Sun, SABER turns 180° approximately every 60 days, performing a yaw manoeuvre. As a result of the yaw, SABER spatial coverage alternates approximately every 60 days from 84°S–52°N to 52°S–84°N. This results in limited data coverage in the high latitudes. The SABER data used in this paper are pre-processed v2.0 global (84°S–84°N) nighttime zonal means of ozone, [H], [O] and temperature on a 4°-latitude grid at 88 pressure levels on a daily basis. The data were averaged between 6 a.m. and 6 p.m. local time. In order to ensure nighttime conditions, only latitudes where the SZA was  $>100^\circ$  at 100 km

during the 12-h averaging period were used. Data in the high-latitude regions of the summer hemisphere, which are affected by permanent sunlight, are excluded from the analysis and are represented as blank regions in the figures. The analysis in this study covers January 2002–December 2019. For further information on the retrieval of the species, readers are referred to the following scientific references: Mlynarczyk et al.<sup>37,38</sup> for [H] and [O], Dawkins et al.<sup>39</sup> and Rong et al.<sup>40</sup> for T and ozone.

Due to the orbit parameters, there is a daily shift in measurement time, introducing a local solar time (LST) drift. This can be potentially problematic for nighttime ozone data, as ozone exhibits slight variations along different LSTs at night<sup>16</sup>. To mitigate this, we used MLS nighttime ozone data, measured at the same LST, to cross-check SABER results, especially the ones in the winter hemisphere higher than 52° latitude, where DJF (JJA) data are limited to JF (JA) due to the yaw effect.

### MLS

The MLS instrument onboard the EOS Aura satellite observes the thermal microwave emissions from the limb of the atmosphere, providing ozone volume mixing ratios from the radiance measurements near 240 GHz. This study utilises MLS v5.0x ozone data<sup>41</sup>, which extends the useful vertical range from 0.02 hPa ( $\sim 70$  km) in v4.2x to 0.001 hPa ( $\sim 95$  km), making it possible to study UMLT ozone. Nighttime ozone is selected based on a solar zenith angle  $>100.5^\circ$  to ensure the atmosphere is in darkness from the ground to over 100 km. Subsequently, the data is processed to daily zonal mean at 55 pressure levels from 84°S to 84°N with a 4° interval. The analysis covers October 2004 to May 2023. Compared to SABER data used in this study, the MLS measurements used here cover a longer period while excluding the year 2003 when large substorms occurred. With its global coverage and consistent local measurement time, the MLS instrument is used to confirm that the mid-high latitude data gaps and the LST drift caused by the SABER yaw manoeuvre do not impact the main conclusions about the location of the EPP-induced ozone anomalies at and below  $10^{-3}$  hPa.

### SD-WACCM-X

WACCM-X is an extended version of WACCM that includes the thermosphere and ionosphere up to 500–700 km. Thus, WACCM-X enables realistic simulations of upper atmospheric variability due to lower atmospheric forcing<sup>42</sup>, as well as the solar and geomagnetic influences on the whole atmosphere. Here we use WACCM-X 2.0 simulations with hourly output over the period 2000–2014, made available by NCAR. In this specified dynamic configuration (SD-WACCM-X), the model is constrained by temperature, zonal, and meridional winds from NASA’s Modern-Era Retrospective Analysis for Research and Application (MERRA-2)<sup>43</sup> below  $\sim 50$  km and by geomagnetic forcing in the form of the Kp index<sup>44</sup>. Above 60 km, the model is fully interactive and free-running. The processed model output used here consists of the daily means of temperature and meridional and vertical components of the residual MMC ( $\bar{v}^*$  and  $\bar{w}^*$ ) in the transformed Eulerian mean (TEM) formalism.  $\bar{v}^*$  and  $\bar{w}^*$  are expressed in a two-dimensional velocity streamfunction  $\bar{\Psi}^*$ , which is computed by the latitudinal integration of the vertical component  $\bar{w}^*$  as in Orsolini et al.<sup>26</sup>.

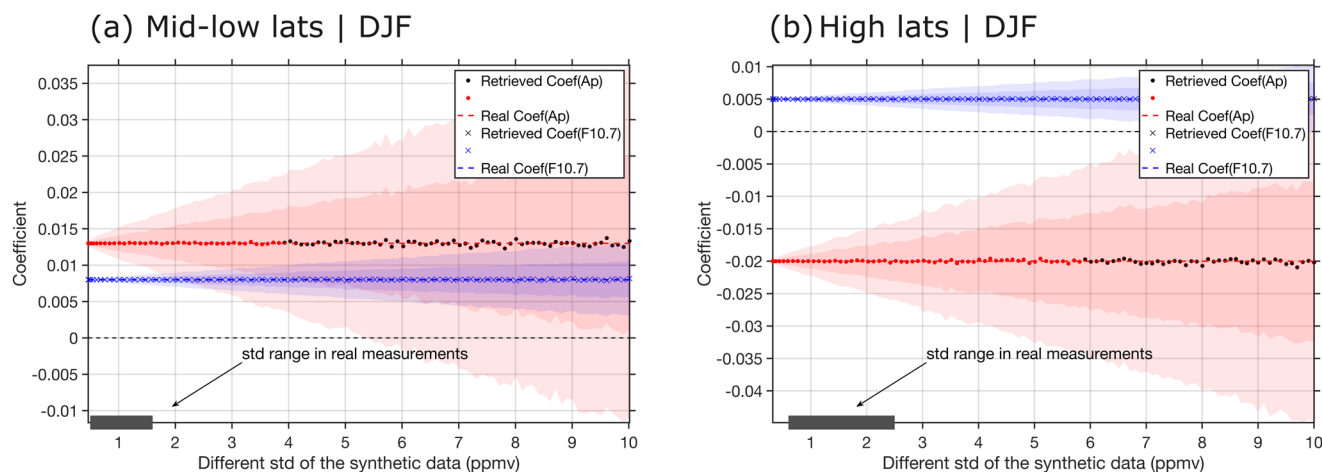


**Fig. 6 | Synthetic test of EPP-induced secondary ozone response using the MLR method: sensitivity to the synthetic data ‘noise’.** **a** Mid-low latitude and **b** high latitude. The black dashed line represents a value of 0. The red and blue dashed lines represent the actual coefficients of Ap and F10.7 in  $\text{Ap}^{-1}$  and  $\text{sfu}^{-1}$ . The dots and

crosses indicate the mean values of the retrieved 1000 coefficients obtained under the same standard deviation levels for Ap and F10.7. The shaded areas represent the confidence levels of 67% and 95%.

## NLRMSIS

The NRLMSIS 2.0 model<sup>35</sup> is an empirical model providing information on the temperature, density and atmospheric composition from the ground to the exobase. This information is based on the day of the year, solar flux, and Ap index input. In this study, the MSIS climatology is generated by MSIS using mean values during the winter time (DJF) of 2002–2023. To expedite computational speed, we have employed a sparse longitude grid of  $20^\circ$  and utilised it for zonal mean calculations. The Ap and F10.7 inputs are set as constant values representing the mean during the targeted period, specifically, 13 for Ap and 100 sfu for F10.7. For details on the chemical reactions considered in the model, interested individuals are referred to Emmert et al.<sup>21</sup>. Notably, ozone is not a standard output of the model. The ozone profiles in the secondary layer region are calculated from  $[\text{O}]$ ,  $[\text{O}_2]$ ,  $[\text{H}]$ , temperature, and air density output from MSIS, assuming nighttime equilibrium (1).

## F10.7 and Ap index

The daily solar radio-flux density at 10.7 cm, i.e., the F10.7 index, is employed to characterise variations in solar cycle radiance. F10.7 is expressed in solar flux units (sfu), where  $1 \text{ sfu} = 10^{-22} \text{ W m}^{-2} \text{ Hz}^{-1}$ . To quantify the extent of EPP entering the atmosphere, we use the geomagnetic activity daily index Ap. This choice is motivated by the rapid response of the UMLT circulation to EPP. The daily Ap index, ranging from 0 to 400, is derived from the three-hourly Ap planetary index. Ap is established as a reliable indicator of EPP. It has been commonly employed in studying the coupling between EPP and the lower atmosphere. The Ap index predominantly reflects electrons, encompassing both auroral electrons (energy  $< 10 \text{ keV}$ ) and MEE (energy between  $10 \text{ keV}$  to several MeV). In this study, we do not aim to differentiate between auroral electrons and MEE. However, we acknowledge that an alternative choice could be considered.

## Research method

Traditionally, the impact of EPP on ozone has been studied by subtracting ozone levels during low geomagnetic activity conditions (Low-Ap) from those during high geomagnetic activity conditions (High-Ap). Due to the fact that the geomagnetic activity is at its strongest during solar maximum and the declining phase of the solar cycle (Fig. S3a and b), this method has limitations due to the inability to account for solar irradiance changes. In the UMLT, the radiation, dynamics, and chemistry are largely driven by solar radiation. The secondary ozone layer is known to be affected by soft X-ray, solar EUV and UV irradiance variability, in particular throughout both the 11-year solar cycle and the 27-day solar rotation cycle<sup>22</sup>. It is thus crucial to

separate the contributions of EPP from those of solar irradiance when examining its effects on secondary ozone.

In this paper, we have employed the multiple linear regression (MLR) method to separate the effects of EPP on secondary ozone and other species from those induced by solar irradiance changes. The climatology of the targeted species was formed on a daily basis by averaging all data available for a particular day, and this was subtracted from the original data on a day-by-day basis to remove seasonal variations. To mitigate the well-known influence of major sudden stratospheric warmings (SSW) in the northern winter hemisphere, we exclude days when the UMLT region could be affected by SSWs, specifically from 5 days before the onset to 15 days after the onset<sup>21</sup>. Following these adjustments, we then fit the values using both the F10.7-index and Ap-index simultaneously. Since the F10.7-index and Ap-index are partly correlated with a maximum correlation of approximately 0.21, we first conducted a series of synthetic tests to evaluate the performance of the MLR method in detecting EPP-induced variations in secondary ozone, in which the F10.7-index and Ap-index were fitted with random noise added. These tests were performed for the winter hemispheric mid/low latitudes (Figs. 6 and 7a) and high latitudes (Figs. 6 and 7b), respectively. By comparing the coefficients obtained from the MLR analysis with the known synthetic input, we observed a high degree of agreement, indicating the robustness and reliability of the MLR method employed in this research:

Figure 6 illustrates the sensitivity of the MLR-derived EPP contribution to natural random variations. In these tests, synthetic data was generated by incorporating the contributions of Ap and F10.7 indices using predefined coefficients (real coefficients), i.e., the coefficients we derived from SABER measurements using the MLR method. Random noise was added to the data to introduce different levels of standard deviation. For each noise level, the test was repeated 1000 times to create a set of synthetic data with the same standard deviation. The MLR method was then applied to each set of synthetic data to estimate the coefficients associated with Ap and F10.7.

When more than 80% of the 1000 retrieved coefficient values reached a 95% confidence level, as determined through the MLR analysis applying a Student’s *t*-test, the mean retrieved values were colour-coded for clarity: red for Ap and blue for F10.7. Coefficients for which more than 20% of the retrieved values did not reach the 95% confidence level were marked in black, indicating lower reliability. The shaded regions illustrate the variability introduced by the random noise, indicating the range of coefficient values at confidence levels of 67% and 95%. The secondary ozone data obtained from real measurements exhibit variations ranging from 0.6 to 2.5 ppmv in the winter polar regions and from 0.5 to 1.6 ppmv in the mid and low latitudes of the winter hemisphere. These variations are represented



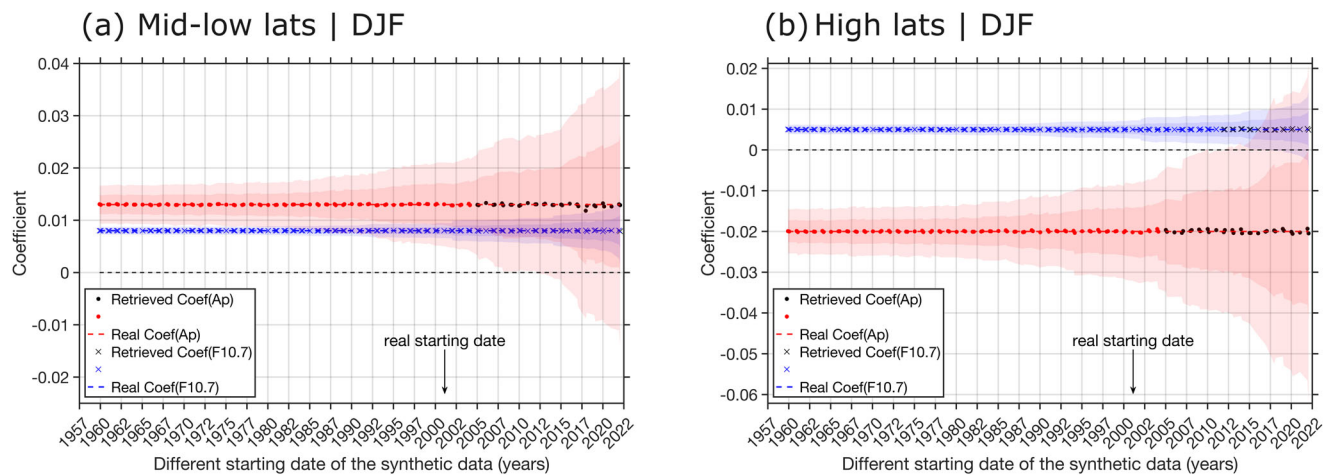


**Fig. 7 | Synthetic test of EPP-induced secondary ozone response using MLR method: sensitivity to the length of synthetic data.** **a** Mid-low latitudes and **b** high latitudes. The black dashed line represents a value of 0. The red and blue dashed lines represent the actual coefficients of Ap and F10.7. The dots and crosses indicate the

mean values of the retrieved 100 coefficients obtained under the same standard deviation levels for Ap and F10.7. The shaded areas represent the confidence levels of 67% and 95%.

by the dark grey rectangles on the  $x$ -axis. Considering these levels of variations, the MLR method can robustly derive the EPP contribution with uncertainty in the coefficient of maximum  $\pm 0.005 \text{ Ap}^{-1}$ .

In addition, we evaluated the MLR results' sensitivity to the length of measurements. While maintaining a realistic standard deviation based on actual measurements and the same ending date of the indices (beginning of 2023), we varied the starting date of the indices from 1960 to 2023. Similar to the previous test, this analysis was repeated 1000 times for each length of synthetic data. The statistical outcomes of the retrieved coefficient values associated with Ap and F10.7 are presented in Fig. 7. As anticipated, the quality of the fitting decreased as the length of measurements was shortened. To maintain a 95% confidence level, the measurement frame needed to be at least 17 years (2005 winter–2022 winter) to be able to detect ozone response to EPP on a seasonal scale. The satellite measurements utilised in our study met this threshold requirement.

### Data availability

TIMED SABER data are available from the website <http://saber.gats-inc.com/data.php>. MLS ozone data used in this study are publicly available at Goddard Earth Sciences Data and Information Services Center (GES DISC), Accessed: 3 July 2023, <https://doi.org/10.5067/Aura/MLS/DATA2516>. Daily geomagnetic activity Ap-index and daily solar flux F10.7-index are publicly available from the German Research Centre for Geosciences (GFZ) website (<https://kp.gfz-potsdam.de>). The CESM2.0 SD-WACCM-X hourly data is accessed through Earth System Grid and is publicly available from [https://www.earthsystemgrid.org/dataset/ucar.cgd.cesm4.f.e20.FXSD.f19\\_f19.001.html](https://www.earthsystemgrid.org/dataset/ucar.cgd.cesm4.f.e20.FXSD.f19_f19.001.html)

### Code availability

The multiple linear regression (MLR) is available as a function in advanced programming languages such as Matlab and Python.

Received: 2 October 2023; Accepted: 25 April 2024;

Published online: 20 May 2024

### References

1. Turunen, E. et al. Impact of different energies of precipitating particles on  $\text{NO}_x$  generation in the middle and upper atmosphere during geomagnetic storms. *J. Atmos. Sol.-Terr. Phys.* **71**, 1176–1189 (2009).
2. Rozanov, E., Calisto, M., Egorova, T., Peter, T. & Schmutz, W. Influence of the precipitating energetic particles on atmospheric chemistry and climate. *Surv. Geophys.* **33**, 483–501 (2012).
3. Sinnhuber, M., Nieder, H. & Wieters, N. Energetic particle precipitation and the chemistry of the mesosphere/lower thermosphere. *Surv. Geophys.* **33**, 1281–1334 (2012).
4. Sinnhuber, M. & Funke, B. Energetic electron precipitation into the atmosphere. In *The Dynamic Loss of Earth's Radiation Belts* (eds Jaynes, A. & Usanova, M.) 279–321 (Elsevier: Amsterdam, The Netherlands, 2020).
5. Thorne, R. M. The importance of energetic particle precipitation on the chemical composition of the middle atmosphere. *PAGEOPH* **118**, 128–151 (1980).
6. Randall, C. E. et al. Stratospheric effects of energetic particle precipitation in 2003–2004. *Geophys. Res. Lett.* **32**, L05802 (2005).
7. Randall, C. E. et al. Energetic particle precipitation effects on the Southern Hemisphere stratosphere in 1992–2005. *J. Geophys. Res.* **112**, D08308 (2007).
8. Andersson, M. et al. Missing driver in the Sun–Earth connection from energetic electron precipitation impacts mesospheric ozone. *Nat. Commun.* **5**, 5197 (2014).
9. Jia, J., Kero, A., Kalakoski, N., Szelag, M. E. & Verronen, P. T. Is there a direct solar proton impact on lower-stratospheric ozone? *Atmos. Chem. Phys.* **20**, 14969–14982 (2020).
10. Smith, A. K., Espy, P. J., López-Puertas, M. & Tweedy, O. V. Spatial and temporal structure of the tertiary ozone maximum in the polar winter mesosphere. *J. Geophys. Res.: Atmos.* **123**, 4373–4389 (2018).
11. Verronen, P. T. & Lehmann, R. Analysis and parameterisation of ionic reactions affecting middle atmospheric  $\text{HO}_x$  and  $\text{NO}_y$  during solar proton events. *Ann. Geophys.* **31**, 909–956 (2013).
12. Smith-Johnsen, C. et al. Nitric oxide response to the April 2010 electron precipitation event: using WACCM and WACCM-D with and without medium-energy electrons. *J. Geophys. Res.: Space Phys.* **123**, <https://doi.org/10.1029/2018JA025418> (2018).
13. Guttu, S., Orsolini, Y., Stordal, F., Limpasuvan, V. & Marsh, D. R. WACCM simulations: decadal winter-to-spring climate impact on middle atmosphere and troposphere from medium energy electron precipitation. *J. Atmos. Sol.-Terr. Phys.* **209**, 105382 (2020).
14. Nilsen, K. et al. Sensitivity of middle atmospheric ozone to solar proton events: comparison between climate model and satellites. *J. Geophys. Res.-Atmos.* <https://doi.org/10.1029/2021JD034549> (2021).
15. Szelag, M. E. et al. Ozone impact from solar energetic particles cools the polar stratosphere. *Nat. Commun.* **13**, 6883 (2022).
16. Smith, A. K. & Marsh, D. R. Processes that account for the ozone maximum at the mesopause. *J. Geophys. Res.* **110**, D23305 (2005).

17. Burkholder, J. B. et al. *Chemical Kinetics and Photochemical Data for Use in Atmospheric Studies, Evaluation No. 19*. JPL Publication 19-5 (Jet Propulsion Laboratory, Pasadena, 2019).
18. Smith, A. K. et al. Satellite observations of high nighttime ozone at the equatorial mesopause. *J. Geophys. Res.* **113**, D17312 (2008).
19. Smith, A. K. et al. Nighttime ozone variability in the high latitude winter mesosphere. *J. Geophys. Res. Atmos.* **119**, 13,547–13,564 (2015).
20. Tweedy, O. V. et al. Nighttime secondary ozone layer during major stratospheric sudden warmings in specified-dynamics WACCM. *J. Geophys. Res. Atmos.* **118**, <https://doi.org/10.1002/jgrd.50651> (2013).
21. Forbes, J. M. Dynamics of the thermosphere. *J. Meteorol. Soc. Jpn. Ser. II* **85B**, 193–213 (2007).
22. Lee, J. N. & Wu, D. L. Solar cycle modulation of nighttime ozone near the mesopause as observed by MLS. *Earth Space Sci.* **7**, <https://doi.org/10.1029/2019EA001063> (2020).
23. Andrews, D. G., Holton, J. R. & Leovy, C. B. *Middle Atmosphere Dynamics* Vol. 40 (Academic Press, 1987).
24. Qian, L., Burns, A. & Yue, J. Evidence of the lower thermospheric winter-to-summer circulation from SABER CO<sub>2</sub> observations. *Geophys. Res. Lett.* **44**, 10100–10107 (2017).
25. Qian, L. & Yue, J. Impact of the lower thermospheric winter-to-summer residual circulation on thermospheric composition. *Geophys. Res. Lett.* **44**, 3971–3979 (2017).
26. Orsolini, Y. J., Zhang, J. & Limpasuvan, V. Abrupt change in the lower thermospheric mean meridional circulation during sudden stratospheric warmings and its impact on trace species. *J. Geophys. Res.: Atmos.* **127**, e2022JD037050 (2022).
27. Wang, J. C. et al. The lower thermospheric winter-to-summer meridional circulation: 1. Driving mechanism. *J. Geophys. Res.: Space Phys.* **127**, e2022JA030948 (2022).
28. Shimazaki, T. The photochemical time constants of minor constituents and their families in the middle atmosphere. *J. Atmos. Terr. Phys.* **46**, 173–191 (1984).
29. Brasseur, G. P. & S. Solomon. *Aeronomy of the Middle Atmosphere* 3rd edn. (Springer, Dordrecht, Netherlands, 2005).
30. Smith, A. K., Marsh, D. R., Mlynczak, M. G. & Mast, J. C. Temporal variations of atomic oxygen in the upper mesosphere from SABER. *J. Geophys. Res.* **115**, D18309 (2010).
31. Jones, M. Jr et al. Coupling from the middle atmosphere to the exobase: Dynamical disturbance effects on light chemical species. *J. Geophys. Res.: Space Phys.* **125**, <https://doi.org/10.1029/2020JA028331> (2020).
32. Xu, J. et al. An observational and theoretical study of the longitudinal variation in neutral temperature induced by aurora heating in the lower thermosphere. *J. Geophys. Res. Space Phys.* **118**, 7410–7425 (2013).
33. Liu, X. et al. Responses of lower thermospheric temperature to the 2013 St. Patrick's Day geomagnetic storm. *Geophys. Res. Lett.* **45**, 4656–4664 (2018b).
34. Wei, G. et al. Temperature variations in the mesosphere and lower thermosphere during geomagnetic storms with disparate durations at high latitudes. *Universe* **9**, 86 (2023).
35. Emmert, J. T. et al. NRLMSIS 2.0: a whole atmosphere empirical model of temperature and neutral species densities. *Earth Space Sci.* **7**, e2020EA001321 (2020).
36. Wang, J. C. et al. The lower thermospheric winter-to-summer meridional circulation: 2. Impact on atomic oxygen. *J. Geophys. Res.: Space Phys.* **128**, <https://doi.org/10.1029/2023JA031684> (2023).
37. Mlynczak, M. G. et al. Atomic hydrogen in the mesopause region derived from SABER: algorithm theoretical basis, measurement uncertainty, and results. *J. Geophys. Res.: Atmos.* **119**, 3516–3526 (2014).
38. Mlynczak, M. G., Hunt, L. A., Russell, J. M. & Marshall, B. T. Updated SABER night atomic oxygen and implications for SABER ozone and atomic hydrogen. *Geophys. Res. Lett.* **45**, 5735–5741 (2018).
39. Dawkins, E. C. M. et al. Validation of SABER v2.0 operational temperature data with ground-based lidars in the mesosphere-lower thermosphere region (75–105 km). *J. Geophys. Res.: Atmos.* **123**, 9916–9934 (2018).
40. Rong, P. P. et al. Validation of thermosphere ionosphere mesosphere energetics and dynamics/sounding of the atmosphere using broadband emission radiometry (TIMED/SABER) v1.07 ozone at 9.6 μm in altitude range 15–70 km. *J. Geophys. Res.* **114**, D04306 (2009).
41. Schwartz, M., Froidevaux, L., Livesey, N. & Read, W. *MLS/Aura Level 2 Ozone (O<sub>3</sub>) Mixing Ratio V005 2020* (Goddard Earth Sciences Data and Information Services Center (GES DISC), Greenbelt, MD, USA, accessed 3 July 2023); <https://doi.org/10.5067/Aura/MLS/DATA2516>.
42. Liu, H.-L. et al. Development and validation of the Whole Atmosphere Community Climate Model with thermosphere and ionosphere extension (WACCM-X 2.0). *J. Adv. Model. Earth Syst.* **10**, 381–402 (2018).
43. Gelaro, R. et al. The modern-era retrospective analysis for research and applications, version 2 (MERRA-2). *J. Clim.* **30**, 5419–5454 (2017).
44. Roble, R. G. & Ridley, E. C. An auroral model for the NCAR thermosphere general circulation model (TGCM). *Ann. Geophys.* **5A**, 369–382 (1987).

## Acknowledgements

J.J., Y.J.O. and P.J.E. are funded by the Research Council of Norway under CoE Contract 223252/F50.

## Author contributions

Y.J.O. and P.J.E. conceived the initial project and research plans, which led to the MSc theses of L.E.M. and T.L. at NTNU. C.C.J.H.S., J.N.L. and D.W. provided the satellite measurements. J.J. designed and led the MLR analysis and improved the satellite data processing. J.J. also designed thorough analyses with L.C.G.Z. performing them using the MSIS model and satellite data (shown in Supplementary Note 2). J.Z. calculated and provided the WACCM-X stream function. J.J. led the writing, with major input from Y.J.O. and P.J.E., and further input from all coauthors.

## Funding

Open access funding provided by Norwegian University of Science and Technology.

## Competing interests

The authors declare no competing interests.

## Additional information

**Supplementary information** The online version contains supplementary material available at <https://doi.org/10.1038/s43247-024-01419-2>.

**Correspondence** and requests for materials should be addressed to Jia Jia.

**Peer review information** *Communications Earth & Environment* thanks Thomas Reddmann and the other, anonymous, reviewer(s) for their contribution to the peer review of this work. Primary Handling Editors: Kerstin Schepanski and Clare Davis. A peer review file is available.

**Reprints and permissions information** is available at <http://www.nature.com/reprints>

**Publisher's note** Springer Nature remains neutral with regard to jurisdictional claims in published maps and institutional affiliations.

**Open Access** This article is licensed under a Creative Commons Attribution 4.0 International License, which permits use, sharing, adaptation, distribution and reproduction in any medium or format, as long as you give appropriate credit to the original author(s) and the source, provide a link to the Creative Commons licence, and indicate if changes were made. The images or other third party material in this article are included in the article's Creative Commons licence, unless indicated otherwise in a credit line to the material. If material is not included in the article's Creative Commons licence and your intended use is not permitted by statutory regulation or exceeds the permitted use, you will need to obtain permission directly from the copyright holder. To view a copy of this licence, visit <http://creativecommons.org/licenses/by/4.0/>.

© The Author(s) 2024